Reaction Rate Ratios for Recent Fast Metal Experiments with Large Plutonium Masses

Hutchinson, Jesson D.
Alwin, Jennifer Louise
Cutler, Theresa Elizabeth
Gooden, Matthew Edgell
Kleedtke, Noah Andrew
Neudecker, Denise
Thompson, Nicholas William
Weldon, Robert Allen Jr.
Whitman, Nicholas Hunter
Little, Robert Currier

To be published in: Nuclear Science and Engineering

DOI to publisher's version: 10.1080/00295639.2024.2343118

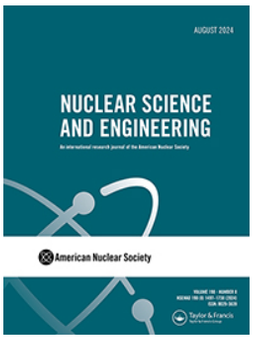

Nuclear Science and Engineering

ISSN: (Print) (Online) Journal homepage: www.tandfonline.com/journals/unse20

Reaction Rate Ratios for Recent Fast Metal Experiments with Large Plutonium Masses

Jesson Hutchinson, Jennifer Alwin, Theresa Cutler, Matthew Gooden, Noah Kleedtke, Denise Neudecker, Nicholas Thompson, Robert Weldon, Nicholas Whitman & Robert Little

To cite this article: Jesson Hutchinson, Jennifer Alwin, Theresa Cutler, Matthew Gooden, Noah Kleedtke, Denise Neudecker, Nicholas Thompson, Robert Weldon, Nicholas Whitman & Robert Little (05 Jun 2024): Reaction Rate Ratios for Recent Fast Metal Experiments with Large Plutonium Masses, Nuclear Science and Engineering, DOI: 10.1080/00295639.2024.2343118

To link to this article: https://doi.org/10.1080/00295639.2024.2343118

NUCLEAR SCIENCE AND ENGINEERING
DOI: https://doi.org/10.1080/00295639.2024.2343118

Reaction Rate Ratios for Recent Fast Metal Experiments with Large Plutonium Masses

Jesson Hutchinson,* Jennifer Alwin, Theresa Cutler, Matthew Gooden, Noah Kleedtke, Denise Neudecker, Nicholas Thompson, Robert Weldon, Nicholas Whitman, and Robert Little

Los Alamos National Laboratory, P.O. Box 1663, MS B228, Los Alamos, New Mexico 87545

Received December 17, 2023
Accepted for Publication April 9, 2024

Abstract — *Reaction rate ratios are integral responses that are used within the criticality experiments field because they contain spectral information. While these types of measurements have been utilized for nuclear data validation with historic experiments, few experiments of this type have been utilized for recent experiments, as few exist. This work focuses on measured reaction rate ratios for two nearly bare plutonium critical assemblies with different geometries: one that is cube like (with a Pu mass of 40 kg) and one that is slab like (with a Pu mass of 109 kg). Irradiations were performed with both configurations in which foils were placed near the center of the assembly. Plutonium, highly enriched uranium, depleted uranium, and Au foils were included in the irradiation and counted via high-purity germanium detectors. From these measurements, reaction rate ratios were calculated.*

Measured and simulated values and uncertainties are presented for the reaction rate ratios. Ratios utilizing the following reactions are given in this work: ^{197}Au(n, γ), ^{197}Au(n,2n), ^{235}U(n,fission), ^{238}U(n, fission), ^{238}U(n,2n), ^{238}U(n,γ), and ^{239}Pu(n,fission). Uncertainties for the measured reaction rate ratios ranged from 4% to 7%, and the contribution of various parameters to this uncertainty was investigated. The results are compared to historical experiments and should be used for nuclear data validation for future nuclear data library releases. These measurements are part of the EUCLID (Experiments Underpinned by Computational Learning for Improvements in Nuclear Data) project, which utilizes measurement responses in addition to k_{eff} (such as these reaction rate ratios) to help reduce uncertainties in ^{239}Pu nuclear data.

Keywords — *Reaction rate ratios, spectral index, criticality experiments, plutonium nuclear data, nuclear data validation.*

Note — *Some figures may be in color only in the electronic version.*

*E-mail: jesson@lanl.gov

I. INTRODUCTION

Reaction rate ratios (RRRs) have been utilized for nuclear data validation for many decades, and continue to be used to this day.[1–6] These ratios provide spectral information about the system being measured that cannot be obtained using k_{eff} measurements alone. Several such reaction rate experiments that feed into nuclear data validation were executed in the 1950s. Recent work further investigated those experiments, including simulations to determine the sensitivities of these responses to nuclear data.[7] One interesting conclusion of that work was that the sensitivities of RRRs to nuclear data are quite different from k_{eff} sensitivities, even on the same system (such as the Jezebel experiment).[8]

When looking at k_{eff} sensitivities, fission and neutron multiplicity $\bar{\nu}$ always trend similarly, but sensitivities to the same nuclear data for RRRs are very different. The sensitivities of RRR to $\bar{\nu}$ are orders of magnitude smaller than to fission cross sections, for instance, while the k_{eff} sensitivities to $\bar{\nu}$ and the (n,f) cross sections are always similar (within a factor of 2). This difference in sensitivities is why the use of RRRs can potentially help constrain nuclear data more than k_{eff} alone, and why these types of measurements can be useful.

The Experiments Underpinned by Computational Learning for Improvements in Nuclear Data (EUCLID) project[9,10] focused on reducing the uncertainty in ^{239}Pu nuclear data from 0.1 to 5 MeV. Specifically, the project aimed to reduce compensating errors between different ^{239}Pu nuclear data. The EUCLID experiment was designed using machine learning to achieve this goal, while obeying constraints associated with available nuclear material.[11] The result of the experiment design was two configurations with different geometries. The first configuration (referred to as 3 × 2) is cube like (5.979 × 6.004 × 7.488 in.) with a Pu mass of 40 kg. The second configuration (referred to as 8 × 1) is slab like (15.944 × 3.002 × 15.093 in.) and has a Pu mass of 109 kg.

For the EUCLID experiment, six responses were measured: RRRs, reactivity coefficients,[12,13] Rossi-α,[14–16] neutron leakage spectra,[17] subcritical experiments,[18] and critical experiments. This work presents the methodology and results associated with the RRR measurements along with their simulations. Future work will utilize this experiment for nuclear data validation and adjustment to assess their usefulness for constraining ^{239}Pu nuclear data.

This work is outlined as follows. First, the methodology is described in Sec. II. Next, the experiment is described in Sec. III, including details of the experiment design, experiment configurations, experiment irradiations, the foils used, and the detectors used to count the foils. The results, including comparisons to simulations, are presented in Sec. IV. Conclusions and future work are then presented in Sec. V.

II. METHODOLOGY

Foil counting has been used for many decades as a way to assess the reaction rates and/or RRRs that occur within an assembly.[3,19–21] Foils for the desired reaction(s) are loaded into a critical assembly or reactor. The system is then taken critical. The system remains at a set power level until the desired neutron fluence is achieved (i.e., a fluence that allows for desirable counting statistics within the available counting time). The foils are then retrieved for counting. Gamma rays emitted from these foils are generally counted with high-purity germanium (HPGe) detectors so that the resolution is adequate to ensure that only the reaction of interest is being counted. The foils need to have a known mass and composition, which are generally determined prior to irradiation. We applied this methodology to measure the reactions listed in Table I.

In addition to measurements of the foils of interest, two additional measurements were also performed. The first was a measurement with a known source(s) to be used to determine the detector efficiency. This measurement had coverage near all energies of interest for the desired foil reaction photo peaks, and the source was located as close as possible to the same position that the foil was located (any difference in location must be accounted for using a correction factor, which is described later). The second measurement determined the background, which was subtracted from the foil measurement. Note that the detectors used had shielding to suppress the gamma background.

This work largely uses notations consistent with another recent publication to describe the analysis procedure.[22] First the gamma spectra measured with the HPGe detector were analyzed, and the peak area recorded for the gamma-ray photo peak of interest $S_{\gamma,i,k}$ was determined. Next, the number of atoms at the end of irradiation $A_{i,k}$ for reaction i and foil k can be determined via

$$A_{i,k} = \frac{S_{\gamma,i,k}\eta_{\gamma,k}P_{c,k}\frac{t_{real,k}}{t_{live,k}}}{\epsilon_{\gamma,i,k}I_{\gamma,i}e^{-\lambda t_{cool,k}}\left(1-e^{-\lambda t_{real,k}}\right)}\ , \tag{1}$$

where

$\eta_{\gamma,k}$ = attenuation correction factor

$P_{c,k}$ = position correction factor during gamma counting

$\epsilon_{\gamma,i,k}$ = absolute detector efficiency

$I_{\gamma,i}$ = branching ratio of the gamma ray associated with the photo peak of interest

λ = decay constant

t_{cool} = cooling/decay time after the irradiation

t_{real} = real time of the measurement

t_{live} = live time of the measurement (the live time is the real time minus the total dead time that occurred during the measurement).

TABLE I

Parameters of Measured Reactions

Reaction	Fission Product[a]	Half-Life (h) $[ln(2)/\lambda]$	Photo Peak Energy (keV)	Branching Ratio, I_γ	Fission Product Yield (γ)[a]
^{197}Au(n,γ)^{196}Au	N/A	64.7	411.8	0.9562	N/A
^{197}Au(n,2n)^{196}Au	N/A	148.0	333.0	0.229	N/A
^{197}Au(n,2n)^{196}Au	N/A	148.0	355.7	0.87	N/A
^{58}Ni(n,p)^{58}Co	N/A	1700.6	810.8	0.9945	N/A
^{58}Ni(n,2n)^{57}Ni	N/A	35.6	1377.6	0.817	N/A
^{54}Fe(n,p)	N/A	7492.8	834.8	0.99976	N/A
^{235}U fission	^{95}Zr	1536.8	756.7	0.5438	0.0643
^{235}U fission	^{97}Zr	16.7	743.4	0.9309	0.0600
^{235}U fission	^{99}Mo	65.9	739.5	0.122	0.0594
^{235}U fission	^{103}Ru	941.9	497.1	0.91	0.0324
^{235}U fission	^{132}Te	76.9	228.2	0.88	0.0466
^{235}U fission	^{140}Ba	306.1	537.3	0.2439	0.0598
^{235}U fission	^{147}Nd	263.5	531.0	0.1311	0.0214
^{239}Pu fission	^{95}Zr	1536.8	756.7	0.5438	0.0482
^{239}Pu fission	^{99}Mo	65.9	739.5	0.122	0.0609
^{239}Pu fission	^{103}Ru	941.9	497.1	0.91	0.0659
^{239}Pu fission	^{132}Te	76.9	228.2	0.88	0.0500
^{239}Pu fission	^{140}Ba	306.1	537.3	0.2439	0.0527
^{239}Pu fission	^{147}Nd	263.5	531.0	0.1311	0.0215
^{238}U fission	^{95}Zr	1536.8	756.7	0.5438	0.0514
^{238}U fission	^{99}Mo	65.9	739.5	0.122	0.0617
^{238}U fission	^{103}Ru	941.9	497.1	0.91	0.0628
^{238}U fission	^{140}Ba	306.1	537.3	0.2439	0.0582
^{238}U fission	^{147}Nd	263.5	531.0	0.1311	0.0259
^{238}U(n,γ)^{239}Np[b]	N/A	56.5	277.6	0.1451	N/A
^{238}U(n,2n)^{237}U	N/A	56.5	208.0	0.212	N/A

[a]N/A = Not applicable.
[b]The direct reaction is ^{238}U(n,γ)^{239}U. This then undergoes inverse beta decay resulting in ^{239}Np. A photo peak from ^{239}Np radioactive decay is then measured.

The reason that an attenuation correction factor $\eta_{\gamma,k}$ is needed is that the foils may have a thickness such that there is self-shielding within the foil. The position correction factor $P_{c,k}$ is needed to correct for slight differences in the placement of the calibration source and the foil being counted.

The reaction rate per gram $R_{i,j,k}$ for a measured reaction i (such as a fission product), inferred reaction j (such as ^{235}U fission), and foil k is given as

$$R_{i,j,k} = \frac{A_{i,k} F_k}{m_k Y_{i,j}} \quad , \tag{2}$$

where m is the mass for foil k, $Y_{i,j}$ is the fission product yield, and F_k is a fission correction factor related to foil purity [i.e., a highly enriched uranium (HEU) foil, not a ^{235}U foil]. For foils with cladding present, m_k does not include the cladding mass. The term $Y_{i,j}$ is set to 1 for nonfission reactions.

Substituting Eq. (1) into Eq. (2) results in

$$R_{i,j,k} = \frac{S_{\gamma,i,k}\eta_{\gamma,k}P_{c,k}\frac{t_{real,k}}{t_{live,k}}F_k}{\epsilon_{\gamma,i,k}I_{\gamma,i}e^{-\lambda t_{cool,k}}(1-e^{-\lambda t_{real,k}})m_k Y_{i,j}} \quad . \tag{3}$$

The RRR is then a ratio of two reaction rates, given as

$$\frac{R_{i,j,k,n}}{R_{i,j,k,d}} = \frac{S_{\gamma,i,k,n}\eta_{\gamma,k,n}P_{c,k,n}\frac{t_{real,k,n}}{t_{live,k,n}}F_{k,n}\epsilon_{\gamma,i,k,d}I_{\gamma,i,d}e^{-\lambda t_{cool,k,d}}(1-e^{-\lambda t_{real,k,d}})m_{k,d}Y_{i,j,d}}{S_{\gamma,i,k,d}\eta_{\gamma,k,d}P_{c,k,d}\frac{t_{real,k,d}}{t_{live,k,d}}F_{k,d}\epsilon_{\gamma,i,k,n}I_{\gamma,i,n}e^{-\lambda t_{cool,k,n}}(1-e^{-\lambda t_{real,k,n}})m_{k,n}Y_{i,j,n}} \quad , \tag{4}$$

where n refers to the numerator and d is for the denominator. For this work, the ^{235}U fission cross section was usually chosen as the reaction in the denominator (i.e., all ratios are some reaction divided by the ^{235}U fission cross section). This particular reaction was used here, as employing this denominator is standard practice in nuclear data validation. A subset of the results in Sec. IV includes other reactions in the denominator.

Often many of these terms are further simplified and referred to as correction factors. This reduces Eq. (1) to

$$A_{i,k} = \frac{S_{\gamma,i,k}\eta_{\gamma,k}P_{c,k}D_k}{\epsilon_{\gamma,i,k}I_{\gamma,i}M_{cool}M_{real}} \quad , \tag{5}$$

where D_k is a dead-time correction factor ($D_k = \frac{t_{real,k}}{t_{live,k}}$), M_{cool} is a correction factor for decay during the cooling time prior to counting ($M_{cool} = e^{-\lambda t_{cool,k}}$), and M_{real} is a correction factor for decay during the measurement ($M_{real} = (1 - e^{-\lambda t_{real,k}})$).

This can be inserted into the reaction rate definition [Eq. (2)],

$$R_{i,j,k} = \frac{S_{\gamma,i,k}\eta_{\gamma,k}P_{c,k}D_kF_k}{\epsilon_{\gamma,i,k}I_{\gamma,i}M_{cool}M_{real}m_kY_{i,j}} \quad , \tag{6}$$

and also into the ratio equation [Eq. (4)],

$$\frac{R_{i,j,k,n}}{R_{i,j,k,d}} = \frac{S_{\gamma,i,k,n}\eta_{\gamma,k,n}P_{c,k,n}D_{k,n}F_{k,n}\epsilon_{\gamma,i,k,d}I_{\gamma,i,d}M_{cool,d}M_{real,d}m_{k,d}Y_{i,j,d}}{S_{\gamma,i,k,d}\eta_{\gamma,k,d}P_{c,k,d}D_{k,d}F_{k,d}\epsilon_{\gamma,i,k,n}I_{\gamma,i,n}M_{cool,n}M_{real,n}m_{k,n}Y_{i,j,n}} \quad . \tag{7}$$

Propagating uncertainties is easy given the linear form of Eq. (7). The following parameters were included in the uncertainty propagation: $S_{\gamma,i,k}$, $\eta_{\gamma,k}$, $P_{c,k}$, $\epsilon_{\gamma,i,k}$, $I_{\gamma,i}$, m_k, $Y_{i,j}$, and F_k. The other parameters (D_k, M_{cool}, and M_{real}) were assumed to have negligible uncertainty.

One assumption associated with the approach described in this section was that the recorded events within the photo peak were coming from the reaction of interest. It is possible that the events were coming from a different source (a different reaction, a sum peak, etc.). For this work, the combination of photo-peak energies and counting times was chosen to minimize the possible impact of any other reactions. Future work will include methods to improve automation to ensure that events within a photo peak are coming from the desired reaction and/or correct for any events that come from other sources. Another assumption of the approach used here was that the reactions were caused by neutron interactions (instead of photon or other interactions). Future work will include more additional simulations to quantify the validity of this assumption.

III. EXPERIMENT DESCRIPTION

III.A. Experiment Design

Reducing compensating errors in fast ^{239}Pu nuclear data was the goal of the EUCLID experiment design. The specific ^{239}Pu observables targeted included fission, inelastic scattering, elastic scattering, capture, $\bar{\nu}$, and prompt fission neutron spectrum. The D-optimality criterion,[23] which minimizes the log determinant of adjusted nuclear data covariances, was used to optimize the experiment design. This metric helps in screening for unproductive responses and gives a measure of information content. Gaussian process optimization was used to maximize D-optimality.[24,25] The MCNP® code, version 6.2[a] with ENDF/B-VIII.0[6] nuclear data, was utilized in the experiment optimization and design.

The optimization showed that RRRs were useful (as opposed to say an additional critical configuration or some other response), but the optimization was not used to determine which ratios would be utilized (which could be performed in future work). Additional information is provided in previous work regarding the experiment design.[9–11]

[a] MCNP and Monte Carlo N-Particle® are registered trademarks owned by Triad National Security, LLC, manager and operator of Los Alamos National Laboratory. Any third party use of such registered marks should be properly attributed to Triad National Security, LLC, including the use of the designation as appropriate. For the purposes of visual clarity, the registered trademark symbol is assumed for all references to MCNP within the remainder of this paper.

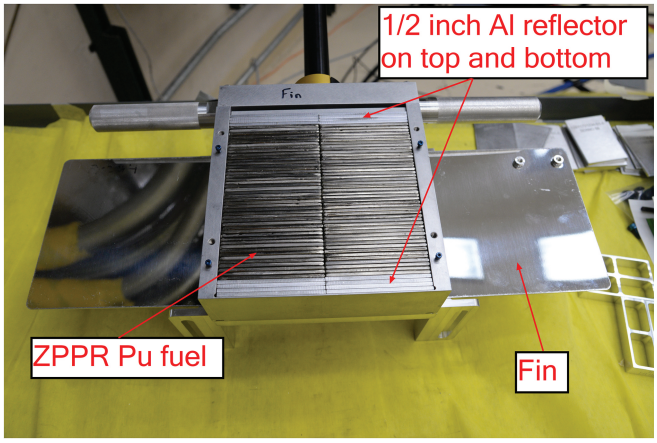

Fig. 1. Single bucket for the 3 × 2 configuration (six total buckets used: three on the bottom movable platen and three on the top stationary platform).

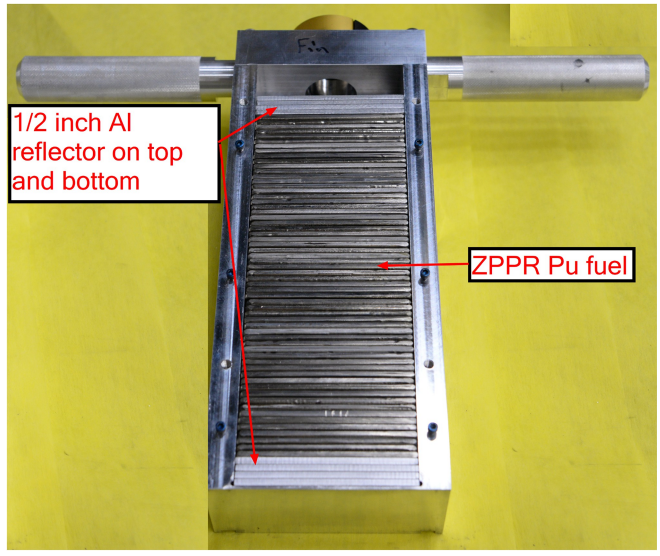

Fig. 2. Single bucket for the 8 × 1 configuration (16 total buckets used: 8 on the bottom movable platen and 8 on the top stationary platform).

III.B. Experiment Configurations

The optimization resulted in two configurations with very different geometries: one was cube like and the other was slab like. Both had rectangular parallelepiped geometry. They used the same fuel, which was made up of zero-power physics reactor (ZPPR) plates, specifically, plutonium-aluminum, no nickel ZPPR plates.[26–30] The average plutonium mass within a plate was 105.383 g.[29] Every ZPPR plate had 304-L stainless steel cladding with outer dimensions of 3.002 × 1.993 × 0.117 in.[29]

The configuration referred to as 3 × 2 had three units in the 1.993-in. dimension, two units in the 3.002-in. dimension, and 64 layers in the 0.117-in. dimension. This resulted in the 3 × 2 configuration having overall dimensions of 5.979 × 6.004 × 7.488 in. The configuration referred to as 8 × 1 had eight units in the 1.993-in. dimension, one unit in the 3.002-in. dimension, and 129 full layers (and a 130th layer with a single ZPPR plate) in the 0.117-in. dimension. This resulted in the 8 × 1 configuration having overall dimensions of 15.944 × 3.002 × 15.093 in.

The ZPPR plates were assembled inside aluminum "buckets." Each bucket was loaded with ZPPR plates, as shown in Fig. 1 for the 3 × 2 configuration and Fig. 2 for the 8 × 1 configuration. These buckets were loaded on the Planet critical assembly machine,[31] shown in Fig. 3 for the 8 × 1 configuration. Planet has a movable platen and a top stationary platform. For this experiment, a core support plate, placed on the stationary platform, was used to support the top fuel while the bottom fuel was on the movable platen. The movable platen can be raised remotely to the desired separation distance (including full closure).

Figures 4 and 5 show slices of the fully assembled 3 × 2 and 8 × 1 configurations, respectively.

Fig. 3. 8 × 1 configuration on the Planet critical assembly machine. Here the platen is in the fully lowered position.

III.C. Experiment Irradiations

In order to have a sufficient number of reactions inside the foils, the required power level in the critical assembly must be raised (referred to in this work as an irradiation). The neutron detection system used to monitor the power level is referred to as the linear channel (LC) system.[32] The LCs are compensated ion chambers with a ^{10}B lining. There were two chambers, and the difference in the ^{10}B lined chamber and the unlined chamber was the neutron current. The power level was proportional to the neutron current (amp) in the LC system. Similarly, the energy was proportional to the neutron current in the LC multiplied by the time (amp·s).

Figures 6 and 7 show the LC current for the 3 × 2 and 8 × 1 irradiations, respectively. As seen in these figures, channel 2 (LC2) consistently had a higher current than the other channels. This is because LC2 was physically closer to the Planet assembly than the other channels. As seen in Fig. 6, the current of LC2 for the 3 × 2 configuration was 1.4E-7 amp during the irradiation and resulted in 1.00E-3 amp·s integrated over the irradiation (7320 s). Similarly, for the 8 × 1 configuration in Fig. 7, the current was 1.3E-7 amp and resulted in 2.34E-3 amp·s integrated over the irradiation (18 000 s). The reason why the larger integrated current was needed for the 8 × 1 compared to the 3 × 2 was because neutron leakage was much

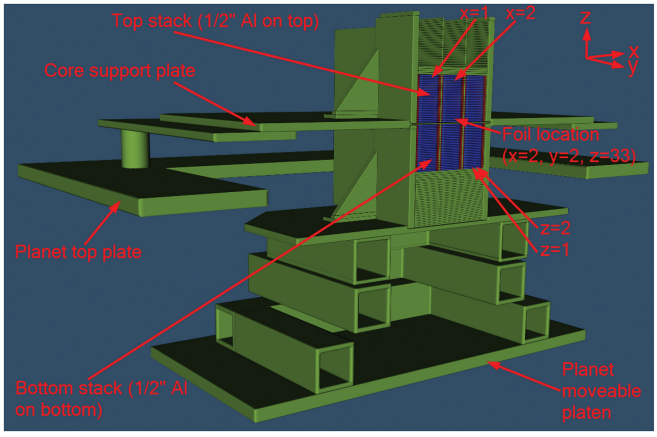

Fig. 4. MCNP model of the 3 × 2 configuration. Color legend: blue is plutonium and green is aluminum 6061-T6. The foil is actually located in $y = 2$ but only $y = 1$ fuel is shown in this slice (so the arrow is showing the correct location in x and z only).

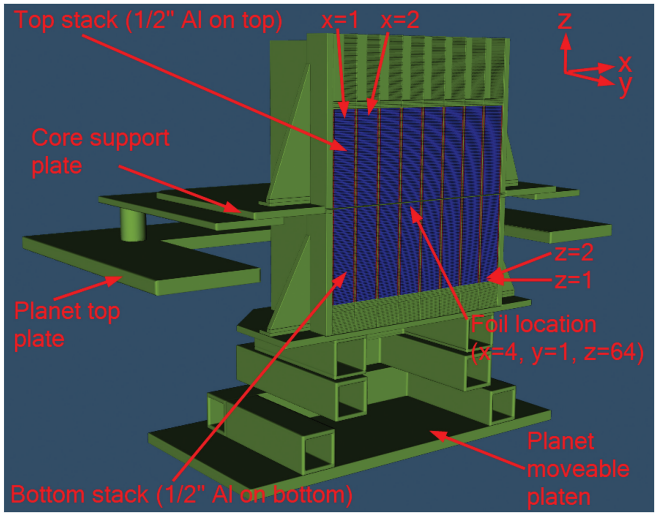

Fig. 5. MCNP model of the 8 × 1 configuration. Color legend: blue is plutonium and green is aluminum 6061-T6.

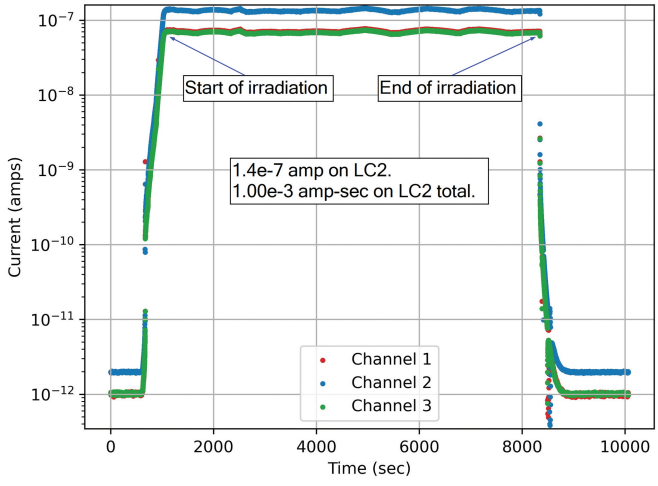

Fig. 6. LC data for the 3 × 2 irradiation.

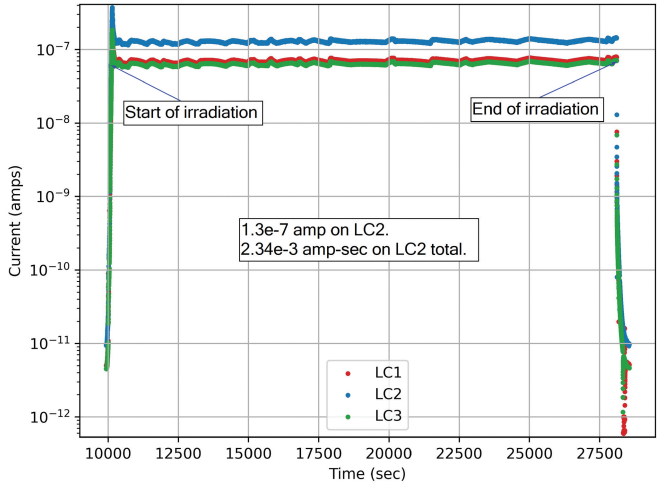

Fig. 7. LC data for the 8 × 1 irradiation.

higher for that configuration (so the total fluence on the foils in both configurations was fairly similar).

III.D. Foil Information

Six foils were irradiated with both configurations: plutonium (Pu), HEU, depleted uranium (DU), gold (Au), nickel (Ni), and iron (Fe). Issues were encountered with the use of the Ni and Fe foils. Specifically, for Fe, it was found that some foils contained significant Mn impurities (even though they were procured at 99.99% pure Fe). The Mn impurity was problematic as the Fe reactions of interest were (n,p) reactions (and therefore, resulted in Mn). For Ni, there were issues encountered with proper counting times due to facility availability. For these reasons, only the results for the other four foils are included in this analysis. Information on the Ni and Fe foils were retained in this section, however, even though no results are reported.

Table II gives the measured masses of each foil m. All foils were nominally 0.5 in. in diameter. The foils used were of the highest purity that could be obtained. The HEU foils were 93.2% ^{235}U (balance assumed to be ^{238}U), the Pu foils were 4.8% ^{240}Pu (balance assumed to be ^{239}Pu), and the DU foils were 0.7% ^{235}U (balance assumed to be ^{238}U). The fission correction factor F_k was calculated using the equation

$$F_k = \frac{\sum \frac{N_x}{N_0}\frac{m_x}{m_0}}{\sum \frac{N_x}{N_0}\frac{\sigma_{f,x}}{\sigma_{f,0}}}, \tag{8}$$

where $\frac{N_x}{N_0}$ is the ratio of the atom fraction of nuclide x to nuclide 0 (the desired nuclide), $\frac{m_x}{m_0}$ is the ratio of atomic masses, and $\frac{\sigma_{f,x}}{\sigma_{f,0}}$ is the ratio of fission cross sections.

TABLE II

Foil Masses m for the EUCLID Irradiations

Material	3 × 2 Mass (mg)	8 × 1 Mass (mg)
Pu	394.24 ± 4.25	432.69 ± 4.65
HEU	63.44 ± 1.41	62.76 ± 1.33
DU	1163.46 ± 21.38	1126.4 ± 21.97
Au	65.43 ± 0.05	126.38 ± 0.05
Ni	285.03 ± 0.05	282.87 ± 0.05
Fe	122.94 ± 0.05	126.48 ± 0.05

These ratios were determined by performing simulations with ENDF/B-VIII.0[6] cross sections using a centralized tally in Jezebel. The sums included all nuclides with a nonzero atom fraction. It should be noted that it was unfortunate that this ratio of fission cross sections was one of the desired outputs of the RRRs, yet those same ratios may also be an input. For this work, that only occurred for the ^{238}U/^{235}U ratio. This is why it is useful to look at additional RRRs instead of always having ^{235}U fission in the denominator (which is investigated in Sec. IV). It should also be mentioned that if the atom fraction of the desired nuclide was high (i.e., $\frac{N_x}{N_0}$ is small for all nuclides when $x \neq 0$), then F_k will be near 1.

Table III shows the fission correction factor values for the Pu, HEU, and DU foils (assumed to be the same for both the 3 × 2 and 8 × 1 irradiations as the foils used were from the same batch of material for each foil type). Note that F_k only applies to fission foils (so for the activation foils, the F_k term was equal to 1 by definition). The F_k term is described in more detail in recent work that reevaluated the RRRs of historical critical experiments.[33]

Figures 8 and 9 show the foil loadout for the 3 × 2 and 8 × 1 configurations, respectively. The foils were loaded in an aluminum sample holder that had the outer dimensions of a ZPPR plate. The sample holder was loaded into the aluminum buckets in a position that was previously occupied by a ZPPR plate. Figure 10 shows the loading of the foil sample holder inside a 3 × 2 bucket. The location of the foil sample holder was nominally near the center for both irradiations, as shown in Figs. 4 and 5.

For the 3 × 2 configuration, the sample plate was loaded in location $x = 2$, $y = 2$, and $z = 33$. This means that it was in the middle location in the x-dimension (number 2 of 3) and the middle location in the z-dimension (layer 33 of 65, which was near the bottom of the top stack). In the y-dimension, it was not possible to center the sample plate, so the choice of $y = 2$ instead of $y = 1$ was arbitrary.

For the 8 × 1 configuration, the sample plate was loaded in location $x = 4$, $y = 1$, and $z = 64$. This resulted in the x-dimension being as centered as possible (number 4 of 8), and the y-dimension always being centered (since there is only 1 unit in the y-dimension). The z-dimension was not perfectly centered (layer 64 of 131); this was chosen as having the sample plate near the top of the bottom stack resulted in significantly lower worker dose rates than having it near the bottom of the top stack during sample retrieval.

TABLE III

Fission Correction Factors F_k

Foil	Desired Nuclide	Weight Percent Nuclide in Foil	Nuclide Ratio	Atom Ratio (m_x/m_0)	σ_f Ratio ($\sigma_{f,x}/\sigma_{f,0}$)	Fission Correction Factor, F_k
Pu	–	–	$^{240}Pu/^{239}Pu$	0.0512	0.69	–
Pu	–	–	$^{241}Pu/^{239}Pu$	0.0032	0.92	–
Pu	^{239}Pu	95.2	–	–	–	1.016
HEU	–	–	$^{234}U/^{235}U$	0.0108	0.93	–
HEU	–	–	$^{236}U/^{235}U$	0.0047	0.50	–
HEU	–	–	$^{238}U/^{235}U$	0.0577	0.30	–
HEU	^{235}U	93.2	–	–	–	1.043
DU	–	–	$^{235}U/^{238}U$	0.0030	3.34	–
DU	^{238}U	99.3	–	–	–	0.993

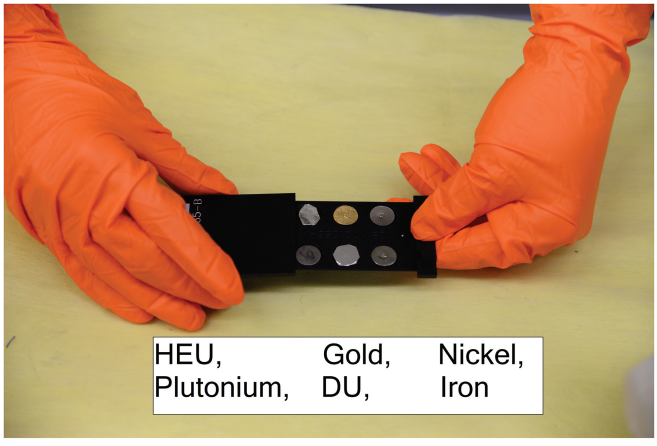

Fig. 8. Foil loadout for the 3 × 2 configuration.

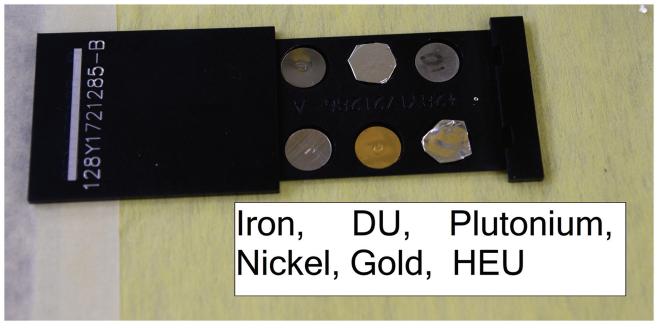

Fig. 9. Foil loadout for the 8 × 1 configuration.

The total number of layers in the z-dimension listed here (65 for the 3 × 2 and 131 for the 8 × 1) are different than those given in Sec. III.B. This is because Sec. III.B gives the specifications of the critical configuration (i.e., with no foil sample holder).

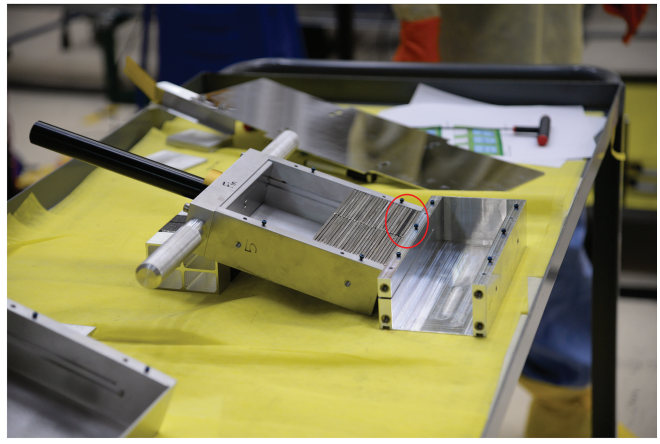

Fig. 10. Location of sample plate holder highlighted in the central 3 × 2 bucket on the top stationary platform.

Since inclusion of the foil sample holder requires removing a ZPPR fuel plate near the center of the assembly, it reduces the reactivity of the system to a subcritical state. In order to make up for this, additional fuel must be added to the top of the assembly. But since the reactivity worth of a ZPPR fuel plate near the center of the assembly is much larger than the worth near the edge of the assembly, more than one plate must be added to overcome the reactivity loss.

For the 3 × 2 configuration, an extra layer of plates was needed (from 64 layers without the sample plate to 65 layers with the sample plate in the location given previously). For the 8 × 1 configuration, the system required 129 full layers with a single ZPPR plate in the 130th layer without a sample plate and 131 full layers with a single ZPPR plate in the 132nd layer with the sample plate.

III.E. Foil Counting

Four HPGe detectors were employed to count the reactions listed in Table I. Figure 11 shows one of the detectors used; note that the shielding was made of lead, but contained a 1-mm tin layer and a 1.5-mm copper layer to suppress lead X-rays. The detector systems had different shielding setups, but all had thick lead shielding to suppress any background radiation (and also to suppress any radiation associated with the other foils).

The foils were all placed onto planchets and had fixed positioning such that the foil center was aligned with the detector crystal center. In addition, the fixed positioning resulted in high precision on the distance from the detector crystal to the foil. One example of this can be seen in Fig. 11.

Prior to conducting these experiments, measurements were performed using a mixed gamma source in each of the same positions from which the foils were measured. This allowed for the efficiency to be determined as a function of energy and position ϵ_γ. It is possible for the position of the foil to be slightly different than the position of the mixed gamma source. If they were different, then the position correction factor P_c would deviate slightly from 1.

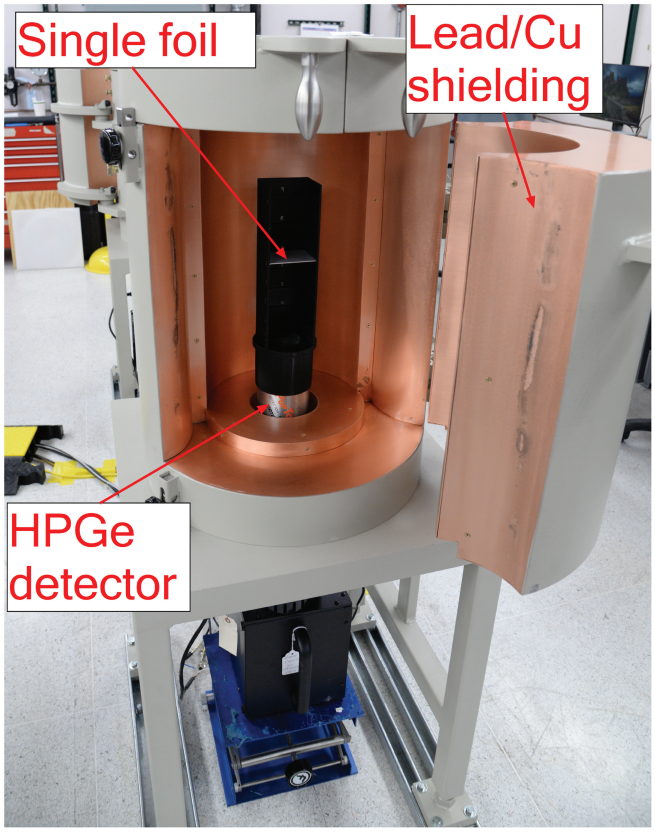

Fig. 11. HPGe detector shown. Foils placed on planchets were located at a known distance from the face of the detector. Lead shielding reduced the background and a tin copper layer shielded lead X-rays.

III.F. Simulations

Simulations were performed of irradiation for both the 3 × 2 and 8 × 1 configurations using MCNP6.2. The MCNP models included the detailed geometry of each ZPPR plate and other experimental components, as shown in Figs. 4 and 5. The ZPPR plate composition used was from the Chlorine Worth Study benchmark.[34]

The MCNP models included the aluminum sample holder, which included cutouts for the foil locations. The individual foils, however, were not included in the model. The volumes that the foils occupied were set as void and were utilized to calculate the desired reaction rates. ENDF/B-VIII.0 nuclear data were utilized for transport; both ENDF-VIII.0 and IRDFF-II (International Reactor Dosimetry and Fusion File)[4] were utilized within the multiplier tallies to calculate the reaction rates.

IV. RESULTS

IV.A. Gamma Spectra

Table I lists all of the reactions that were included in this work. Note that additional photo peaks associated with the reactions listed are also present in the data but were not used. Similarly, additional fission products also could have been used. Both may be included in future work.

Figure 12 shows an example of the gamma spectra collected by the HPGe detectors for the DU foil in the 3 × 2 configuration. Figures 13 and 14 show the same data, but zoomed in on specific photo peaks. In all of these figures, the color corresponds to the time after irradiation (shown in the color legend). Blue is earlier times and green is later times after irradiation.

Some interesting characteristics can be seen when comparing the short-lived example in Fig. 13 [56.544-h half-life for ^{239}Np, created via ^{238}U(n,γ)] versus the long-lived example in Fig. 14 (941.9-h half-life for the fission product ^{103}Ru). It can be seen that the early data (in blue) had a much better signal-to-noise ratio when the half-life was short (Fig. 13) compared to when the half–life was long (Fig. 14). The opposite

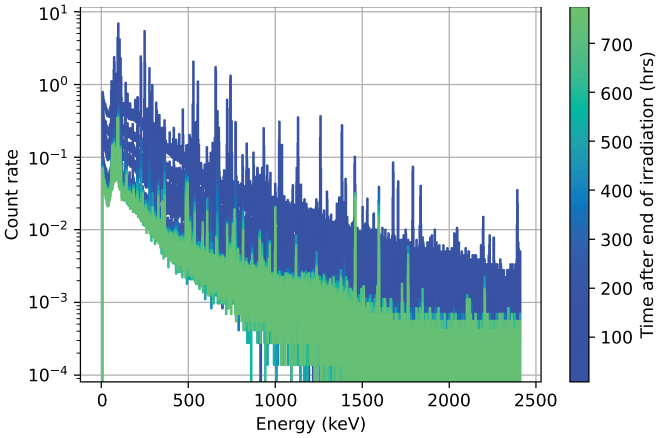

Fig. 12. Gamma spectra of the DU foil for the 3 × 2 configuration.

was true for the late data (in green). Given this, one must be careful in the selection of data that are utilized for analysis of a specific photo peak.

IV.B. RRR Values

Once the proper data were selected and the gamma spectra were analyzed, the approach in Sec. II could be applied. Tables I through IV include the parameters that were applied in the analysis. The individual RRRs were determined via Eq. (4) for each pair of entries in Table I. For the fission RRRs, an average weighted by counting statistics for each fission product in Table I was utilized. Table IV lists ^{133}I, which was used originally but was removed from inclusion due to the large reported uncertainty in the yield given in ENDF/B-VIII.0. This uncertainty was unrealistically high and

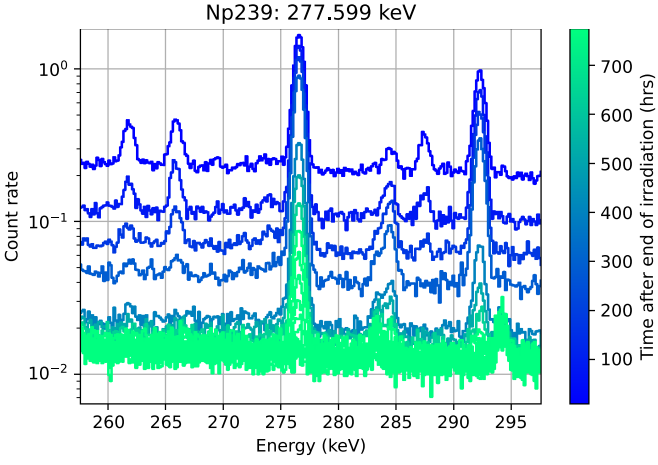

Fig. 13. DU foil for the 3 × 2 configuration zoomed in near the ^{238}U(n,γ)^{239}Np 277.599-keV photo peak. This is an example with a short (56.544-h) half-life.

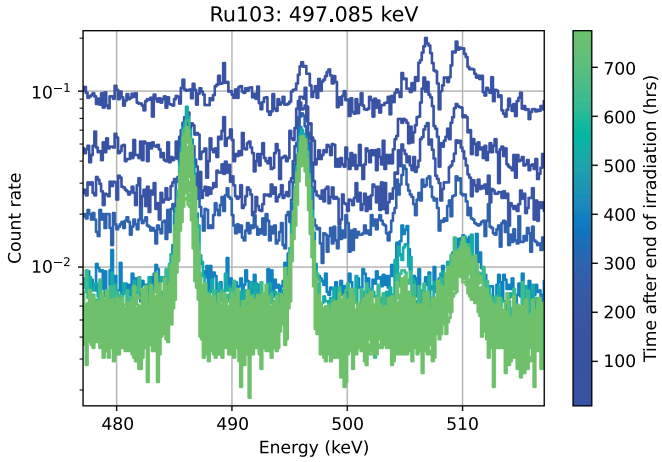

Fig. 14. DU foil for the 3 × 2 configuration zoomed in near the ^{103}Ru fission product photo peak at 497.085 keV. This is an example with a longer (941.9-h) half-life.

has already been updated for inclusion in ENDF/B-VIII.1.[35] Similar to averaging fission products, for ^{196}Au (which has two photo peaks of interest shown in Table I), a weighted average was also utilized. All other reactions only had a single photo peak (and therefore, no averaging was necessary).

The RRR results are shown in Tables V and VI for the 3 × 2 and 8 × 1 configurations, respectively. The propagated measurement uncertainties in these tables included all of the terms listed at the end of Sec. II. The chosen reaction for the denominator in these tables was always ^{235}U fission. It can be seen in the tables that the relative uncertainty in the measured ratios was between 3.9% to 6.9%. The simulated uncertainties included only statistical uncertainties in the Monte Carlo simulation.

The bar chart in Fig. 15 highlights the differences between the measured and simulated results. It can be seen that the measured values were generally greater than the simulated values for the 3 × 2. For the 8 × 1, this was not the case (three ratios had simulated values greater than the experiment values and vice versa). Of the 12 results shown in Figure 15, five have measured and simulated results within one standard deviation (using the reported measured uncertainties in Tables V and VI), four are within one to two standard deviations, one is within two to three standard deviations, and two are more than three standard deviations away.

Figure 16 shows an overlay of the simulated flux versus energy overlaid with the reaction cross sections of interest. The constant difference in flux between

TABLE IV

Fission Product Yields Used for This Work from ENDF/B-VIII.0*

Parent	Fission Product	Yield	Uncertainty	Uncertainty (%)
^{235}U	^{95}Zr	6.4320E-02	6.4320E-04	1.0%
^{235}U	^{97}Zr	6.0003E-02	8.4004E-04	1.4%
^{235}U	^{99}Mo	5.9431E-02	8.3200E-04	1.4%
^{235}U	^{103}Ru	3.2439E-02	4.5415E-04	1.4%
^{235}U	^{132}Te	4.6608E-02	9.3215E-04	2.0%
^{235}U	^{140}Ba	5.9777E-02	5.9777E-04	1.0%
^{235}U	^{147}Nd	2.1389E-02	2.1400E-04	1.0%
^{235}U	^{133}I	6.7179E-02	4.2995E-02	64.0%
^{239}Pu	^{95}Zr	4.8200E-02	1.4940E-03	3.1%
^{239}Pu	^{99}Mo	6.0900E-02	1.8880E-03	3.1%
^{239}Pu	^{103}Ru	6.5919E-02	9.8878E-04	1.5%
^{239}Pu	^{132}Te	4.9995E-02	9.9990E-04	2.0%
^{239}Pu	^{140}Ba	5.2700E-02	1.6340E-03	3.1%
^{239}Pu	^{147}Nd	2.1500E-02	3.6550E-04	1.7%
^{239}Pu	^{133}I	6.6798E-02	4.2750E-02	64.0%
^{238}U	^{95}Zr	5.1405E-02	7.1967E-04	1.4%
^{238}U	^{99}Mo	6.1683E-02	8.6356E-04	1.4%
^{238}U	^{103}Ru	6.2753E-02	8.7855E-04	1.4%
^{238}U	^{140}Ba	5.8152E-02	4.0707E-04	0.7%
^{238}U	^{147}Nd	2.5927E-02	3.6298E-04	1.4%
^{238}U	^{133}I	6.7594E-02	4.3260E-02	64.0%

*Due to its high report uncertainty, ^{133}I was not used in this work.

TABLE V

3 × 2 RRR Results

	Measured			Simulated		
Ratio Name	Value	Uncertainty	Uncertainty %	Value	Uncertainty	Uncertainty %
Au197(n,2n)/U235f	0.0026	0.0002	6.9	0.0021	0.0001	2.5
Au197(n,g)/U235f	0.1018	0.0041	4.0	0.0790	0.0002	0.2
Pu239f/U235f	1.4505	0.0839	5.8	1.4043	0.0023	0.2
U238(n,2n)/U235f	0.0092	0.0005	5.2	0.0087	0.0001	1.2
U238(n,g)/U235f	0.0709	0.0036	5.0	0.0647	0.0001	0.2
U238f/U235f	0.1593	0.0089	5.6	0.1617	0.0004	0.2

the two configurations indicated that fairly similar RRRs were expected between the configurations, especially those utilizing threshold reactions.

As mentioned previously, the presented results for fission used a weighted average of all of the fission products listed in Table I. Table VII shows the individual reaction rate fission results using different fission products. The column labeled "sigma" in this table shows the number of sigma of that fission product from the listed average. It can be seen from this table that the spread among the different fission products was fairly small.

TABLE VI

8 × 1 RRR Results

Ratio Name	Measured			Simulated		
	Value	Uncertainty	Uncertainty %	Value	Uncertainty	Uncertainty %
Au197(n,2n)/U235f	0.0028	0.0002	6.1	0.0025	0.0001	3.5
Au197(n,g)/U235f	0.1083	0.0042	3.9	0.0922	0.0003	0.3
Pu239f/U235f	1.5588	0.0868	5.6	1.4460	0.0037	0.3
U238(n,2n)/U235f	0.0102	0.0005	5.2	0.0104	0.0002	1.6
U238(n,g)/U235f	0.0792	0.0039	5.0	0.0778	0.0002	0.3
U238f/U235f	0.1841	0.0096	5.2	0.1944	0.0006	0.3

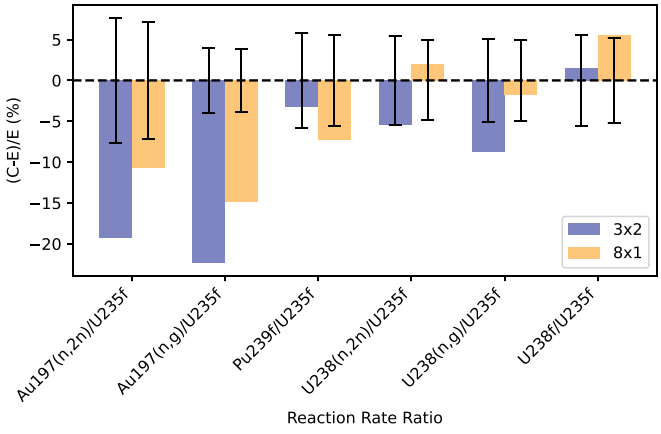

Fig. 15. (C-E)/E comparison between the simulated (C) and measured (E) results for the 3 × 2 and 8 × 1 RRRs.

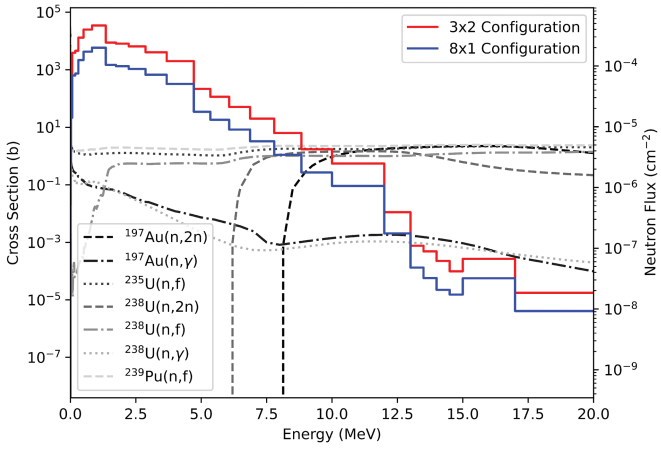

Fig. 16. Simulated neutron flux per source particle for both experimental configurations plotted with select cross sections.

In addition to having ^{235}U fission in the denominator, the results of all possible combinations of RRRs were also investigated. Figure 17 shows the measured results for all combinations of reactions for both configurations. It should be noted that for these results, only ^{147}Nd was used as the fission product (instead of averaging over all fission products). As shown in Table VII, this would result in results similar to averaging all fission products. Figure 18 shows a similar heat map, but compares the measured and simulated results. For the 3 × 2, it can clearly be seen that the results utilizing Au had the largest deviation. For the 8 × 1, ^{197}Au(n,γ) also showed large deviation, but ^{197}Au(n,2n) was clearly in better agreement than the 3 × 2.

IV.C. RRR Uncertainties

Tables V and VI include the uncertainties of each RRR. Using the approach given in Sec. II, individual sources of uncertainty can be isolated. Uncertainties for the following parameters were included: peak area $S_{\gamma,i,k}$, attenuation correction $\eta_{\gamma,k}$, position correction factor during gamma counting $P_{c,k}$, absolute detector efficiency $\epsilon_{\gamma,i,k}$, branching ratio $I_{\gamma,i}$, correction factor related to foil purity F_k, foil mass m_k, and fission product yield $Y_{i,j}$. Uncertainties in the dead-time correction factor D_k and measurement times M_{cool} and M_{real} were assumed to be negligible and were not included. Note that each of the parameters included had an uncertainty associated with the reaction in the numerator as well as in the denominator. Figures 19 through 22 show how each parameter contributed to

TABLE VII

Reaction Rate Results with Different Fission Products

Reaction	Fission Product	3 × 2			8 × 1		
		Value	Uncertainty	Sigma	Value	Uncertainty	Sigma
U235f	^{95}Zr	9.04E+10	3.07E+09	1.0	8.80E+10	2.93E+09	0.2
	^{97}Zr	9.63E+10	3.39E+09	0.8	8.37E+10	2.88E+09	1.7
	^{99}Mo	9.15E+10	3.64E+09	0.6	8.56E+10	3.36E+09	0.9
	^{103}Ru	9.33E+10	3.50E+09	0.1	9.09E+10	3.35E+09	0.7
	^{132}Te	9.79E+10	5.24E+09	0.8	9.49E+10	4.84E+09	1.3
	^{140}Ba	8.93E+10	3.14E+09	1.3	8.60E+10	2.94E+09	0.9
	^{147}Nd	9.59E+10	3.57E+09	0.7	9.16E+10	3.20E+09	0.9
	Average	9.35E+10			8.87E+10		
Pu239f	^{95}Zr	1.24E+11	6.42E+09	1.7	1.42E+11	5.98E+09	0.8
	^{99}Mo	1.43E+11	6.44E+09	1.2	1.34E+11	6.02E+09	0.7
	^{103}Ru	1.37E+11	4.69E+09	0.4	1.39E+11	4.65E+09	0.2
	^{132}Te	1.38E+11	6.73E+09	0.3	1.38E+11	6.74E+09	0.0
	^{140}Ba	1.31E+11	5.53E+09	0.7	1.34E+11	5.62E+09	0.8
	^{147}Nd	1.39E+11	4.75E+09	0.8	1.41E+11	4.73E+09	0.7
	Average	1.35E+11			1.38E+11		
U238f	^{95}Zr	1.45E+10	7.23E+08	0.6	1.59E+10	5.58E+08	0.6
	^{99}Mo	1.52E+10	5.97E+08	0.6	1.61E+10	6.36E+08	0.3
	^{103}Ru	1.48E+10	5.70E+08	0.0	1.62E+10	6.01E+08	0.1
	^{140}Ba	1.51E+10	5.05E+08	0.5	1.64E+10	5.51E+08	0.2
	^{147}Nd	1.47E+10	5.91E+08	0.3	1.67E+10	6.15E+08	0.7
	Average	1.49E+10			1.62E+10		

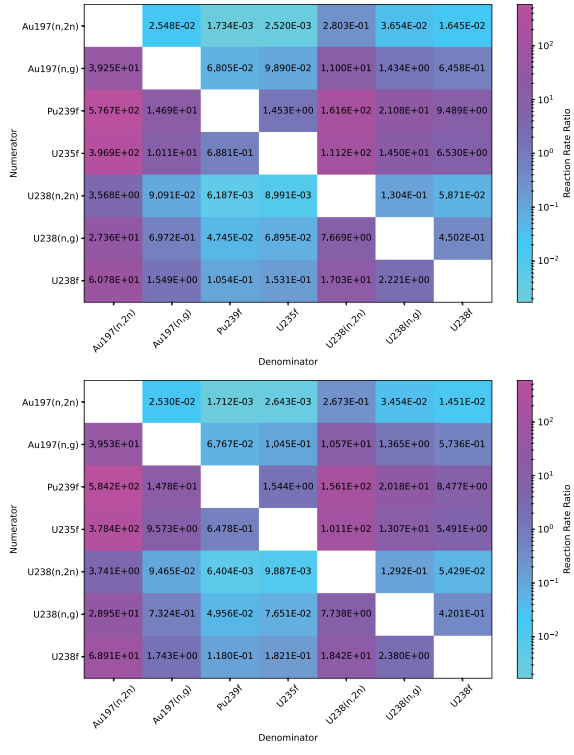

Fig. 17. Heat map with measured RRRs for the 3 × 2 and 8 × 1 configurations.

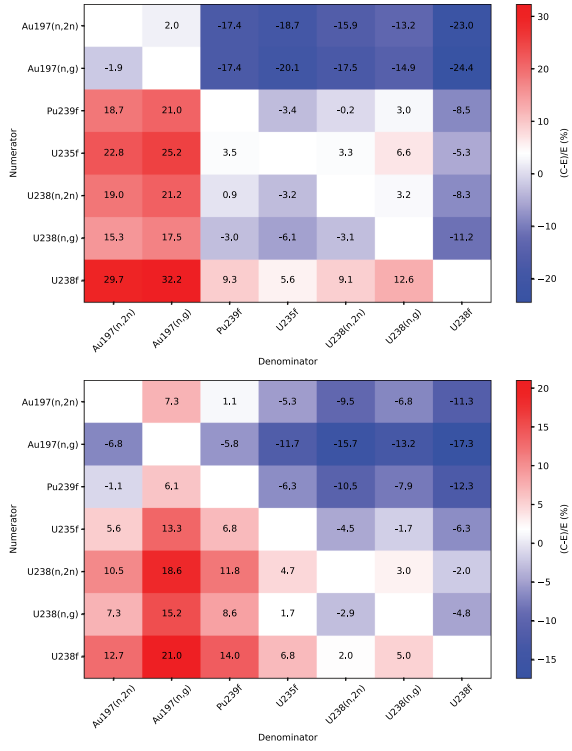

Fig. 18. Heat map with RRR (C-E)/E comparison between the simulated (C) and measured (E) results for the 3 × 2 and 8 × 1 configurations.

the measured absolute uncertainties. In these figures, the uncertainties are stacked in an arbitrary order, but the purpose of these figures is to easily see which parameters contributed the most to the overall uncertainty.

In Figs. 19 through 22, it is easiest to focus on a reaction such as ^{197}Au(n,γ)/^{235}U(n,fission) first, as it had the smallest percent uncertainty in Tables V and VI. What can be seen in Fig. 19 is that the majority of the uncertainty came from the HEU foil, in particular, the mass m_k and foil purity F_k. Since all ratios used ^{235}U(n,fission), the HEU foil essentially set a lower threshold on the overall experiment uncertainty. The Au foil had smaller uncertainties than the HEU, and therefore, the total uncertainty in ^{197}Au(n,γ)/^{235}U(n, fission) was dominated by the HEU. When DU and Pu foils were used, however, their uncertainties were comparable to those of the HEU. In general, it was the mass m_k and foil purity F_k that were the largest contributors to the uncertainty.

For the Pu foil, it was found that the fission product yield $Y_{i,j}$ also contributed significantly. The fission product yield uncertainties that came directly from the ENDF/B-VIII.0[6] nuclear data (for fast fission) are shown in Table IV. As seen in this table, the uncertainties associated with ^{95}Zr, ^{99}Mo, and ^{140}Ba for ^{239}Pu fission were large. These are the fission products that drive the $Y_{i,j}$ uncertainty. As previously stated, ^{133}I was removed from the analysis due to the extremely large uncertainty in this yield in ENDF/B-VIII.0.

In order to reduce uncertainties for future experiments, better foil mass and foil purity information will be needed. While foil mass is generally a straightforward parameter, it is less so for HEU, DU, and Pu foils. For HEU and DU, the foils were

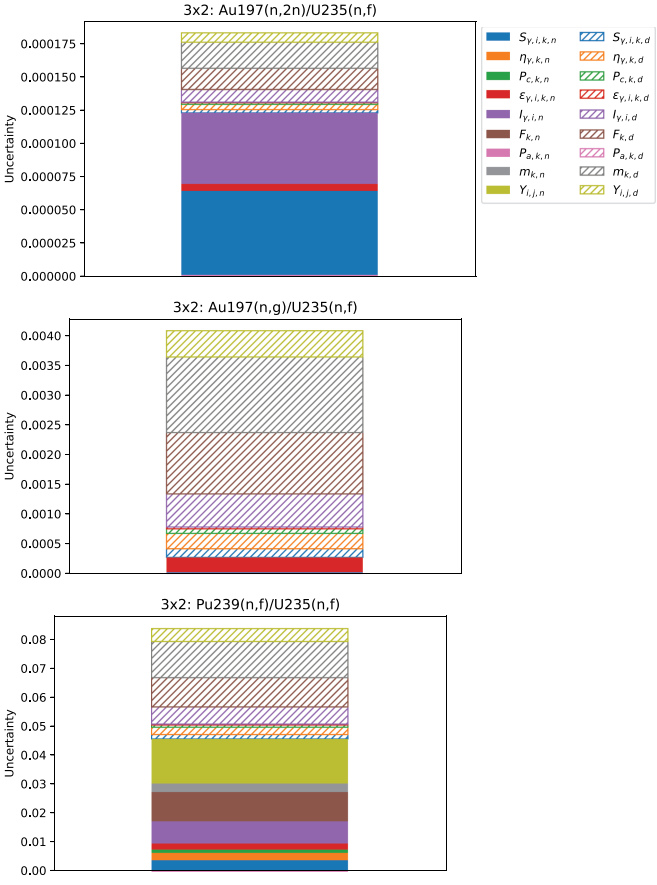

Fig. 19. 3 × 2 reaction rate absolute uncertainty associated with each parameter. Solid colors are uncertainties in the numerator reaction (subscript n) and dashed colors are associated with the denominator reaction [subscript d and always ^{235}U(n,fission)].

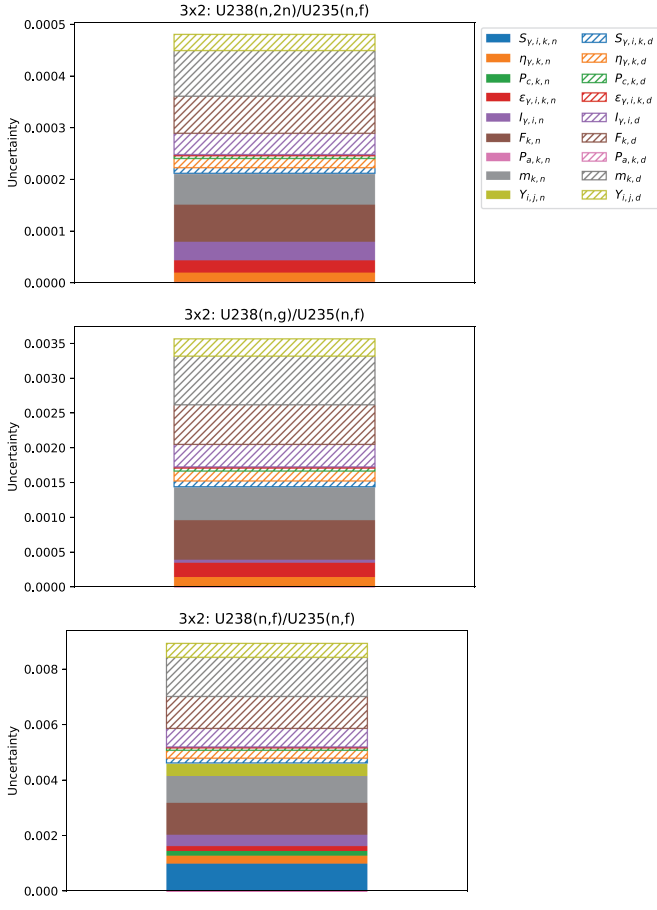

Fig. 20. 3 × 2 reaction rate absolute uncertainty associated with each parameter. Solid colors are uncertainties in the numerator reaction (subscript n) and dashed colors are associated with the denominator reaction [subscript d and always ^{235}U(n,fission)].

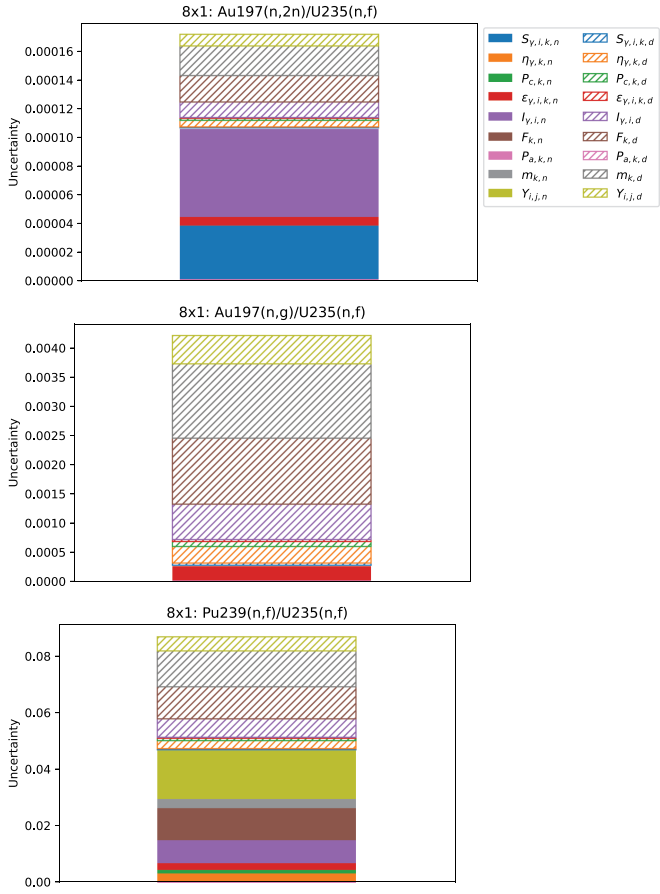

Fig. 21. 8 × 1 reaction rate absolute uncertainty associated with each parameter. Solid colors are uncertainties in the numerator reaction (subscript n) and dashed colors are associated with the denominator reaction [subscript d and always ^{235}U(n,fission)].

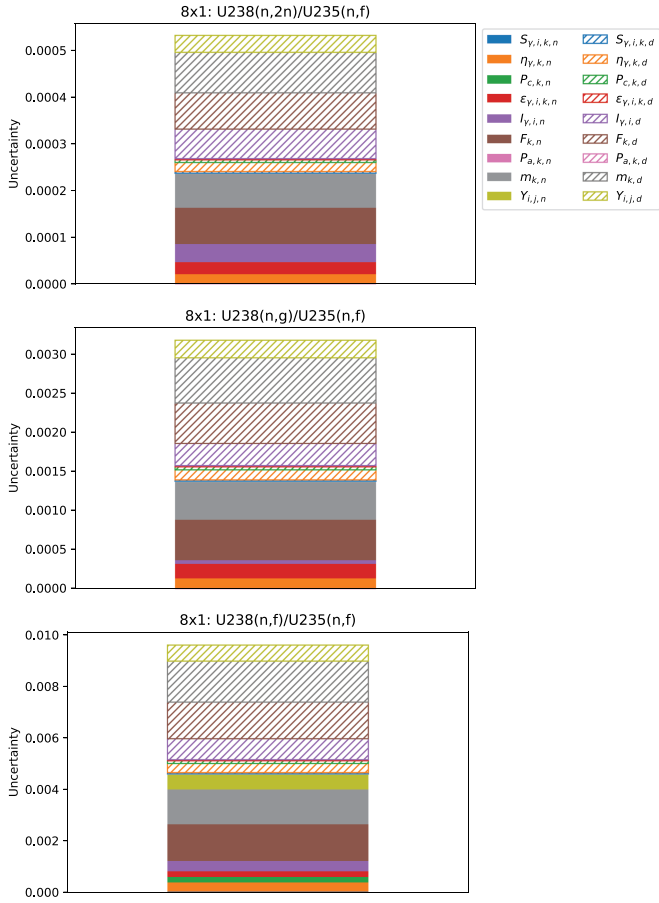

Fig. 22. 8 × 1 reaction rate absolute uncertainty associated with each parameter. Solid colors are uncertainties in the numerator reaction (subscript n) and dashed colors are associated with the denominator reaction [subscript d and always ^{235}U(n,fission)].

bare, and these materials can easily oxidize. While surface oxidation is generally not an issue for large uranium parts, it is an issue when the components become very small like the foils used in this work. For Pu, there was a separate complication in that the foil was clad with 5-mil-thick Ni. Therefore, if the Pu foil is placed on a scale, only the combined (Pu + Ni) mass can be obtained. Both of these issues can be somewhat overcome by the use of gamma spectroscopy prior to irradiation. This, however, will have larger uncertainties than direct mass measurements performed using a precise scale.

IV.D. Comparison to Other Critical Experiments

For all the results presented thus far, the fluences experienced by the various foils were different and a correction for this had not been applied. Such a correction factor was not needed because the simulations accurately represented the difference in fluence. However, in most historical experiments, the fluence was taken to be the same for each of the foils. This was useful to consider when comparing different experiments to one another. Correction factors were made for historical experiments (either through measurements or simulations), or work was performed to demonstrate that a correction factor was not needed (i.e., if the fluence of all foils were shown to be the same). To compare the EUCLID results to those of the historical experiments, a correction factor must be applied.

Here, a position correction factor denoted as $P_{a,k}$ (the subscript a here is due to the location within the assembly) was determined using MCNP simulations. A tally of the fluence was performed and then scaled to that of the ^{235}U foil. The values for P_a are given in

Table VIII. It is not surprising that the deviation from 1 was much larger for the 3 × 2 configuration (minimum of 0.88 and maximum of 1.19) compared to the 8 × 1 configuration (minimum of 0.93 and maximum of 1.08). This occurred because the 3 × 2 configuration was less symmetrical from the point of view of adding a single sample plate to replace a single ZPPR fuel plate. This correction factor is then included in Eq. (2), which becomes

$$R_{i,j,k} = \frac{A_{i,k} F_k P_{a,k}}{m_k Y_{i,j}} \quad . \tag{9}$$

The results are compared to the Jezebel critical experiment (PU-MET-FAST-001)[8] in Fig. 23. Here, Jezebel is shown in the shaded region. Different references have reported slightly different values (and often these changes in values have been larger than the uncertainties given in a specific reference),[8,36–38] which is why a range is shown. Note that the ^{197}Au(n,γ)/^{235}U(n,fission) ratio is not shown as there were no reported values for Jezebel using this ratio. It can be seen that the ^{238}U(n,fission)/^{235}U(n,fission) value for Jezebel is higher than for the EUCLID experiments.

As shown in Table IX, Jezebel had a harder spectrum than both EUCLID experiments, since both the 3 × 2 and 8 × 1 configurations had 1/2-in.-thick aluminum present. Given the harder spectra, it was expected that the ^{238}U(n,fission)/^{235}U(n,fission) ratio would be higher for Jezebel since it is a threshold reaction. Comparison to several historical experiments are shown in Figs. 24 and 25. Note that both the data points and plot for Fig. 24 are from the ENDF/B-VIII.0 validation paper,[6] with the EUCLID points added. In both figures, one ratio is shown on the *y*-axis and a second ratio [always ^{238}U(n,fission)/^{235}U(n,fission)] is shown on the *x*-axis. As seen in both figures, the EUCLID results fall roughly

TABLE VIII

Position Correction Factors P_a

Foil	3 × 2	8 × 1
Pu	0.883 ± 0.001	0.985 ± 0.003
HEU	0.884 ± 0.001	1.014 ± 0.003
DU	0.971 ± 0.002	0.930 ± 0.002
Au	0.971 ± 0.002	0.951 ± 0.002
Ni	1.193 ± 0.002	1.084 ± 0.003
Fe	1.191 ± 0.002	1.053 ± 0.003

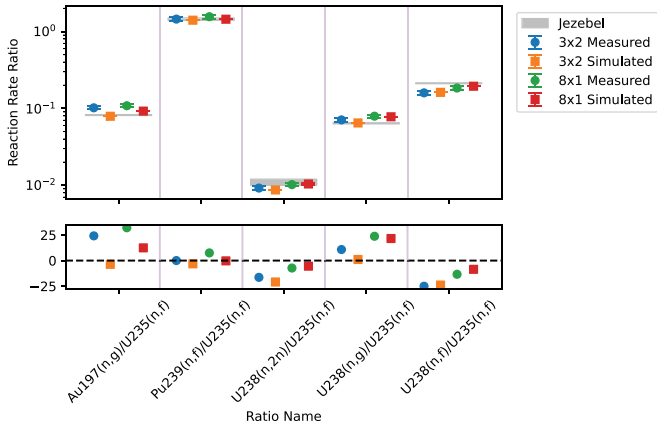

Fig. 23. Comparison between the EUCLID and Jezebel experiments. Jezebel is shown in the gray shaded region. The RRRs are shown in the top plot and the difference (in percent) between EUCLID and Jezebel is shown in the bottom plot.

where one would expect them given that both EUCLID configurations are fast Pu systems (but slightly softer than Jezebel, as shown in Table IX).

V. CONCLUSIONS

The EUCLID experiment included two configurations with very different geometries: one that was cube like (with a Pu mass of 40 kg) and on that was slab like (with a Pu mass of 109 kg). An irradiation was performed on both configurations, each using six foils approximately 0.5 in. in diameter: Pu, HEU, DU, Au, Ni, and Fe. The foils were located near the center of the assembly. After each irradiation, the foils were retrieved within hours and gamma spectroscopy counting was performed using HPGe detectors. The RRRs were presented for ^{197}Au(n,2n)/^{235}U(n,fission), ^{197}Au(n,γ)/^{235}U(n,fission), ^{239}Pu(n,fission)/^{235}U(n,fission), ^{238}U(n,2n)/^{235}U(n,fission), ^{238}U(n,γ)/^{235}U(n,fission), and ^{238}U(n,fission)/^{235}U(n,fission).

Uncertainties for the measured RRRs ranged from 4% to 7%. The uncertainty of individual parameters was investigated, and it was found that the foil mass and purity were the largest contributors to experiment uncertainty. The measured results were compared both to simulations and also to previous experimental work. Differences of 0.2% to 22% were observed between the measurements and simulations, and 5 of the 12 ratios were within one standard deviation of the measured uncertainties.

The results compared well to historical experiments and should be included in future nuclear data validation

TABLE IX

Comparison of Simulated Spectral Characteristics of Jezebel and EUCLID Using MCNP6.2

	Jezebel	3 × 2	8 × 1
Average neutron energy causing fission (MeV)	1.92E+00	1.70E+00	1.70E+00
Percent thermal (<0.625 eV)	0.00%	0.00%	0.00%
Percent intermediate (0.625 eV to 100 keV)	1.89%	2.59%	2.49%
Percent fast (>100 keV)	98.11%	97.41%	97.41%

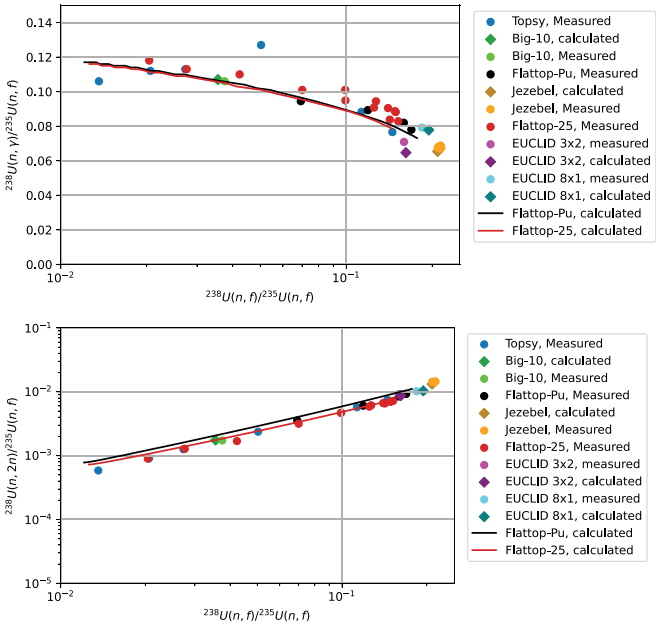

Fig. 24. RRRs for (top) ^{238}U(n,γ)/^{235}U(n,fission) and (bottom) ^{238}U(n,2n)/^{235}U(n,fission). Both have ^{238}U(n,fission)/^{235}U(n,fission) on the *x*-axis. EUCLID results (all on the right side) are added to those presented in previous work.[6]

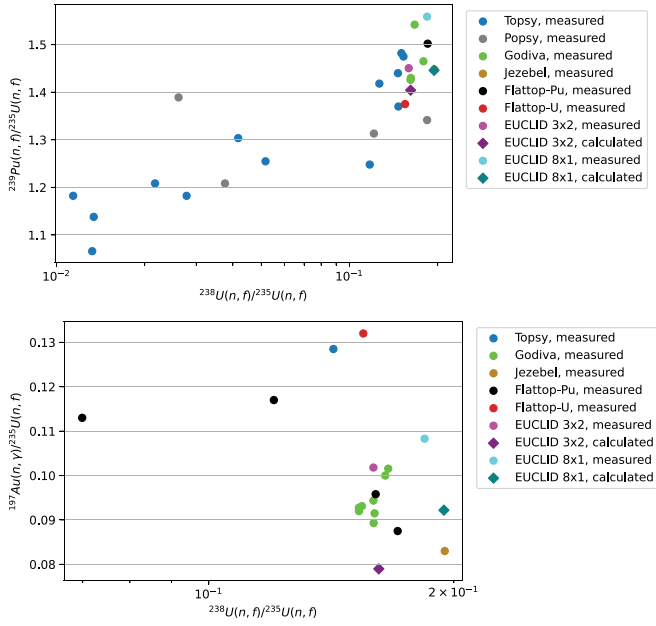

Fig. 25. RRRs for (top) ^{239}Pu(n,fission)/^{235}U(n,fission) and (bottom) ^{197}Au(n,γ)/^{235}U(n,fission). Both have ^{238}U(n,fission)/^{235}U(n,fission) on the *x*-axis. EUCLID results (all on the right side) are added to those presented in previous work.[6]

work. The data from this experiment will also be utilized in future nuclear data adjustment work to help reduce ^{239}Pu compensating errors.

Acknowledgments

Research reported in this paper was supported by the U.S. Department of Energy (DOE) Laboratory Directed Research and Development (LDRD) program at Los Alamos National Laboratory. This work was also supported by the DOE Nuclear Criticality Safety Program, funded and managed by the National Nuclear Security Administration for the DOE. Los Alamos National Laboratory is operated by Triad National Security, LLC, for the National Nuclear Security Administration of the DOE under contract no. 89233218CNA000001.

Disclosure Statement

No potential conflict of interest was reported by the authors.

Funding

This work was supported by the Los Alamos National Laboratory.

ORCID

Jesson Hutchinson http://orcid.org/0000-0001-7364-186X

References

1. P. YOUNG et al., "Evaluation of Neutron Reactions for ENDF/B-VII: $^{232-241}$U and ^{239}Pu," *Nucl. Data Sheets*, **108**, *12*, 2589 (2007); https://doi.org/10.1016/j.nds.2007.11.002.
2. G. PALMIOTTI et al., "Applications of Integral Benchmark Data," *Nucl. Sci. Eng.*, **178**, *3*, 295 (2014); https://doi.org/10.13182/NSE14-33.
3. A. C. KAHLER, M. MACINNES, and M. B. CHADWICK, "A Re-Analysis of Historical Los Alamos Critical Assembly Reaction Rate Measurements," *EPJ Web Conf.*, **106**, 4007 (2016); https://doi.org/10.1051/epjconf/201610604007.
4. A. TRKOV et al., "IRDFF-II: A New Neutron Metrology Library," *Nucl. Data Sheets*, **163**, 1 (2020); https://doi.org/10.1016/j.nds.2019.12.001.
5. C. WILKERSON et al., "A Comparison of Reaction Rate Calculations Using ENDF/B-VII with Critical Assembly Measurements," *Proc. Int. Conf. on Nuclear Data for Science and Technology*, p. 841 (2017); https://doi.org/10.1051/ndata:07332.
6. D. BROWN et al., "ENDF/B-VIII.0: The 8th Major Release of the Nuclear Reaction Data Library with CIELO-Project Cross Sections, New Standards and Thermal Scattering Data," *Nucl. Data Sheets*, **148**, 1 (2018); https://doi.org/10.1016/j.nds.2018.02.001.
7. J. ALWIN et al., "Investigating Fission Reaction Rate Ratio Sensitivities," *Proc. Nuclear Criticality Safety Division Topl. Mtg. (NCSD 2022)*, p. 93 (2022).
8. J. FAVORITE, "Bare Sphere of Plutonium-239 Metal," *International Handbook of Evaluated Criticality Safety Benchmark Experiments*, NEA 7328, Organisation for Economic Co-operation and Development Nuclear Energy Agency (2016); https://doi.org/10.1787/e2703cd5-en.
9. J. HUTCHINSON et al., "EUCLID: A New Approach to Constrain Nuclear Data via Optimized Validation Experiments Using Machine Learning," *EPJ Web of Conf.*, **284**, 15006 (2023); https://doi.org/10.1051/epjconf/202328415006.
10. J. HUTCHINSON et al., "Criticality Experiments to Reduce Compensating Errors in Plutonium Nuclear Data," presented at the Int. Conf. on Nuclear Criticality 2023, Sendai, Japan (2023).
11. I. MICHAUD et al., "Expert-in-the-Loop Optimized Critical Experiments: Reducing Compensating Error in Nuclear Data," presented at the Conf. on Data Analysis (CODA) (2023).
12. T. CUTLER et al., "Reactivity Coefficient Measurements and Sensitivity Studies," *Proc. Nuclear Criticality Safety Division Topl. Mtg. (NCSD 2022)*, p. 85 (2022).
13. T. CUTLER et al., "Validation of Jezebel Reactivity Coefficients and Sensitivity Analysis," *Trans. Am. Nucl. Soc.*, **125**, *1*, 627 (2022).
14. N. KLEEDTKE et al., *Data Assimilation Using Non-invasive Monte Carlo Sensitivity Analysis of Reactor Kinetics Parameters*, Vol. 284, p. 15009, LA-UR-22-27233, Los Alamos National Laboratory (2022); https://www.epj-conferences.org/articles/epjconf/abs/2023/10/epjconf_nd2023_15009/epjconf_nd2023_15009.html
15. N. KLEEDTKE et al., "Sensitivity Coefficients Calculated for the Prompt Neutron Decay Constant At or Near Delayed Critical," *Proc. Nuclear Criticality Safety Division Topl. Mtg. (NCSD 2022)*, p. 685 (2022).
16. N. KLEEDTKE, W. HAECK, and J. HUTCHINSON, "Utilization of Nuclear Data Toolkit ACEtk to Calculate Relative Sensitivity Coefficients of Point-Kinetics Parameters," *Submitted Ann. Nucl. Energy*, **193**, 110031 (2023); https://doi.org/10.1016/j.anucene.2023.110031.
17. N. THOMPSON et al., "Neutron Leakage Spectra Sensitivities for ICSBEP Benchmarks," *Trans. Am. Nucl. Soc.*, **127**, *1*, 646 (2022).
18. A. R. CLARK et al., "How Can a Diverse Set of Integral and Semi-Integral Measurements Inform Identification of Discrepant Nuclear Data?," *EPJ Web of Conf.*, **284**, 15004 (2023); https://doi.org/10.1051/epjconf/202328415004.
19. N. D. DUDEY et al., "Fission-Product-Rate Measurements and Yields," *Nucl. Technol.*, **25**, *2*, 294 (1975); https://doi.org/10.13182/NT75-A24370.
20. J. GRUNDL et al., "Measurement of Absolute Fission Rates," *Nucl. Technol.*, **25**, *2*, 237 (1975); https://doi.org/10.13182/NT75-A24366.
21. H. C. PAXTON, "Fast Critical Experiments," *Prog. Nucl. Energy*, **7**, *3*, 151 (1981); https://doi.org/10.1016/0149-1970(81)90030-5.
22. M. STEFANIK et al., "Neutron Spectrum Determination of Accelerator-Driven d(10)+Be Neutron Source Using the Multi-Foil Activation Technique," *Radiat. Phys. Chem.*, **190**, 109767 (2022); https://doi.org/10.1016/j.radphyschem.2021.109767.
23. R. S. JOHN and N. R. DRAPER, "D-optimality for Regression Designs: A Review," *Technometrics*, **17**, *1*, 15 (1975); https://doi.org/10.1080/00401706.1975.10489266.
24. I. MICHAUD et al., "Designing Critical Experiments Using Gaussian Process Optimization," *Trans. Am. Nucl. Soc.*, **121**, *1*, 1035 (2019).

25. D. SIEFMAN et al., "Constrained Bayesian Optimization of Criticality Experiments," *Ann. Nucl. Energy*, **151**, 107894 (2021); https://doi.org/10.1016/j.anucene.2020.107894.

26. R. LELL et al., "ZPPR-21 Phase A: A Cylindrical Assembly of Pu Metal Reflected by Graphite," *International Handbook of Evaluated Criticality Safety Benchmark Experiments*, NEA 7328, Organisation for Economic Co-operation and Development, Nuclear Energy Agency (2016); https://doi.org/10.1787/e2703cd5-en.

27. R. LELL et al., "ZPR-6 Assembly 10: A Cylindrical Plutonium/Carbon/Stainless Steel Assembly with Stainless Steel and Iron Reflectors," *International Handbook of Evaluated Criticality Safety Benchmark Experiments*, NEA 7328, Organisation for Economic Co-operation and Development, Nuclear Energy Agency (2016); https://doi.org/10.1787/e2703cd5-en.

28. R. LELL, "ZPR-3 Assembly 59: A Cylindrical Assembly of Plutonium Metal and Graphite with a Thick Lead Reflector," *International Handbook of Evaluated Criticality Safety Benchmark Experiments*, NEA 7328, Organisation for Economic Co-operation and Development, Nuclear Energy Agency (2016); https://doi.org/10.1787/e2703cd5-en.

29. C. PERCHER, "TEX Plutonium Baseline Assemblies: Plutonium/Aluminum Metal Alloy Plates with Varying Thicknesses of Polyethylene Moderator and a Thin Polyethylene Reflector, PU-MET-MIXED-002," *International Handbook of Evaluated Criticality Safety Benchmark Experiments*, NEA 7328, Organisation for Economic Co-operation and Development, Nuclear Energy Agency (2020).

30. J. GODA et al., "Comparison of Methods for Determining Multiplication in Subcritical Configurations of a Plutonium System," *Proc. PHYSOR 2018*, Cancun, Mexico, April 22 −26, 2018 (2018).

31. R. SANCHEZ et al., "A New Era of Nuclear Criticality Experiments: The First 10 Years of Planet Operations at NCERC," *Nucl. Sci. Eng.*, **195**, *1*, S1 (2021); https://doi.org/10.1080/00295639.2021.1951077.

32. J. HUTCHINSON et al., "Comparison of Approach-to-Critical Results in Current and Pulse Mode for Systems with High Starter Neutron Rates," *Trans. Am. Nucl. Soc.*, **127**, *1*, 638 (2022).

33. A. LEE, "(U)compendium of LANL Historical Critical Assembly Experiments: 1953-1976, A Radiochemistry Reassessment," LA-UR-23-32767, Los Alamos National Laboratory (2023).

34. J. FAVORITE and T. CUTLER, "Thermal-Spectrum Critical Assemblies with a Polyvinyl Chloride and Chlorinated Polyvinyl Chloride-Plutonium-Aluminum Metal Alloy Core Surrounded by a Polyethylene Reflector," *International Handbook of Evaluated Criticality Safety Benchmark Experiments*, NEA 7328, Organisation for Economic Co-operation and Development, Nuclear Energy Agency (2023).

35. A. MATTERA and A. A. SONZOGNI, "Revision of Fission Yields Uncertainties in ENDF/B-VIII.0," BNL-220804-2021-INRE, Brookhaven National Laboratory (2021); https://doi.org/10.2172/1762758.

36. G. JARVIS et al., "Two Plutonium-Metal Critical Assemblies," *Nucl. Sci. Eng.*, **8**, *6*, 525 (1960); https://doi.org/10.13182/NSE60-A25840.

37. L. B. ENGLE, G. E. HANSEN, and H. C. PAXTON, "Reactivity Contributions of Various Materials in Topsy, Godiva, and Jezebel," *Nucl. Sci. Eng.*, **8**, *6*, 543 (1960); https://doi.org/10.13182/NSE60-A25842.

38. G. HANSEN and H. PAXTON, "Specifications of Los Alamos Fast-Neutron Assemblies in the CSEWG Benchmark Format," LA-UR-79-2923, Los Alamos National Laboratory (1979).